tvst

Article

Metal Oxide Engineered Nanomaterials Modulate Rabbit Corneal Fibroblast to Myofibroblast Transformation

Atsuhiko Fukuto[1,2,*], Soohyun Kim[1,*], Jennifer Kang[1], Brooke L. Gates[1], Maggie W. Chang[1], Kent E. Pinkerton[3,5], Laura S. Van Winkle[3,5], Yoshiaki Kiuchi[2], Christopher J. Murphy[1,4], Brian C. Leonard[1], and Sara M. Thomasy[1,4]

[1] Department of Surgical and Radiological Sciences, School of Veterinary Medicine, University of California-Davis, Davis, CA, USA
[2] Department of Ophthalmology and Visual Sciences, Graduate School of Biomedical Sciences, Hiroshima University, Hiroshima, Japan
[3] Center for Health and the Environment, University of California-Davis, Davis, CA, USA
[4] Department of Ophthalmology & Vision Science, School of Medicine, University of California-Davis, Davis, CA, USA
[5] Department of Anatomy, Physiology and Cell Biology, School of Veterinary Medicine, University of California-Davis, Davis, CA, USA

Correspondence: Sara M. Thomasy, University of California-Davis, 1 Shields Avenue, Davis, CA 95616, USA. e-mail: smthomasy@ucdavis.edu

Received: April 8, 2021
Accepted: August 31, 2021
Published: October 18, 2021

Keywords: engineered nanomaterial; KFM transformation; keratocyte; corneal stroma; corneal wound healing; nanotoxicity

Citation: Fukuto A, Kim S, Kang J, Gates BL, Chang MW, Pinkerton KE, Van Winkle LS, Kiuchi Y, Murphy CJ, Leonard BC, Thomasy SM. Metal oxide engineered nanomaterials modulate rabbit corneal fibroblast to myofibroblast transformation. Transl Vis Sci Technol. 2021;10(12):23, https://doi.org/10.1167/tvst.10.12.23

Purpose: Corneal keratocyte-fibroblast-myofibroblast (KFM) transformation plays a critical role in corneal stromal wound healing. However, the impact of engineered nanomaterials (ENMs), found in an increasing number of commercial products, on this process is poorly studied. This study investigates the effects of metal oxide ENMs on KFM transformation in vitro and in vivo.

Methods: Cell viability of rabbit corneal fibroblasts (RCFs) was tested following treatment with 11 metal oxide ENMs at concentrations of 0.5 to 250 µg/ml for 24 hours. Messenger RNA (mRNA) and protein expression of αSMA, a marker of myofibroblast transformation, were measured using RCFs after exposure to 11 metal oxide ENMs at a concentration that did not affect cell viability, in media containing either 0 or 10 ng/ml of TGF-β1. Additionally, the effect of topical Fe_2O_3 nanoparticles (NPs) (50 ng/ml) on corneal stromal wound healing following phototherapeutic keratectomy (PTK) was determined.

Results: V_2O_5, Fe_2O_3, CuO, and ZnO ENMs were found to significantly reduce cell viability as compared to vehicle control and the other seven metal oxide ENMs tested. V_2O_5 nanoflakes significantly reduced mRNA and protein αSMA concentrations in the presence of TGF-β1. Fe_2O_3 NPs significantly increased αSMA mRNA expression in the presence of TGF-β1 but did not alter αSMA protein expression. Topically applied Fe_2O_3 NPs in an in vivo rabbit corneal stromal wound healing model did not delay healing.

Conclusions: Fe_2O_3 NPs promote corneal myofibroblast induction in vitro but do not impair corneal stromal wound healing in vivo.

Translational Relevance: These experimental results can apply to human nanomedical research.

Introduction

Metal oxide engineered nanomaterials (ENMs) are widely used in consumer products, such as sunscreens and cosmetics, and industrial applications due to their UV-protective and semiconductor properties.[1] Moreover, they are utilized for biomedical cancer therapy[2] and as biosensors.[3] In addition to consumer products, occupational exposure also occurs during the manufacturing of products containing metal oxide ENMs.[4] Direct ocular exposure to metal oxide ENMs in the environment or the workplace can lead to ocular surface damage. Although ample literature exists regarding the cytotoxic effects of metal oxide ENMs on mammalian cells,[5–10] a paucity of research is available regarding their impact on corneal cells, particularly in vivo.[11–14]

The maintenance of a clear and transparent cornea is essential for functional vision, in which the

keratocyte is the key stromal cell. Following corneal injury, quiescent keratocytes transform into fibroblasts, an activated phenotype, which enter into the cell cycle and migrate into the injured area.[15] As wound repair proceeds, fibroblasts differentiate into myofibroblasts that are characterized by the expression of alpha-smooth muscle actin (αSMA). Myofibroblasts are typically larger and contain more actin stress fibers than other fibroblasts.[16] This keratocyte-fibroblast-myofibroblast (KFM) transformation is strongly promoted by transforming growth factor-beta (TGF-β), a cytokine secreted by corneal epithelial cells that can control the behavior of fibroblasts.[17]

In normal wound healing, myofibroblasts disappear from the site of the injury after wound closure and initial remodeling.[18] Importantly, excessive numbers and/or extended persistence of myofibroblasts in the wound space can lead to fibrosis and a loss of corneal transparency, also known as stromal haze.[19]

The toxicity of metal oxide ENMs is thought to be mainly due to the reactive oxygen species (ROS) that they generate, however, direct toxicity through the release of metal ions[20,21] with subsequent damage to the cell and mitochondrial membranes likely also plays a role.[8] Oxidative stress activates the TGF-β-induced transition of fibroblasts to myofibroblasts in various tissues including the cornea.[22–24] We therefore hypothesized that metal oxide ENMs would decrease corneal fibroblast viability, while simultaneously propelling additional fibroblasts to undergo KFM transformation. The present study aimed to examine the viability and fibroblast-to-myofibroblast transformation of corneal fibroblasts in vitro following exposure to each of the following 11 metal oxide ENMs: magnesium oxide (MgO), aluminum oxide (Al_2O_3), titanium oxide (TiO_2) (25 nm and 100 nm), vanadium pentoxide (V_2O_5), iron(III) oxide (Fe_2O_3), copper(II) oxide (CuO), zinc oxide (ZnO), cerium(IV) oxide (CeO_2) (10 nm and 30 nm), and tungsten(VI) oxide (WO_3). We selected these metal oxide ENMs because they are commonly used in commercial and industrial applications.[25] Informed by in vitro results, we tested the effect of topical Fe_2O_3 nanoparticles (NPs) on corneal stromal wound healing using an in vivo rabbit phototherapeutic keratectomy (PTK) model.

Materials & Methods

ENM Synthesis and Characterization and Preparation of Suspensions

The ENMs utilized in this study were produced, synthesized, and/or described by the Engineered Nanomaterials Coordination Core (ERCC) as part of the Nanotechnology Health Implications Research (NHIR) Consortium at the Harvard T.H. Chan School of Public Health. The following gold and metal oxide ENMs were assessed in this study (primary particle diameter in parenthesis): Au (15 nm), MgO (20 nm), Al_2O_3 (30 nm), TiO_2 (25 nm and 100 nm), V_2O_5 (100 nm), Fe_2O_3 (10 nm), CuO (50 nm), ZnO (50 nm), CeO_2 (10 nm and 30 nm), and WO_3 (15 nm). The citrate-capped Au NPs were synthesized following the Turkevich method[26] and characterized by Dong and colleagues.[27] The MgO, TiO_2 (25 nm), TiO_2 (100 nm), V_2O_5, CuO, and ZnO were procured by Strem Chemicals, Inc. (Newburyport, MA), Acros Organics (Carlsbad, CA), Precheza (Přerov, Czech Republic), NanoShel LLC (Wilmington, DE), Sigma Aldrich (St. Louis, MO), and Meliorum Technologies, Inc. (Rochester, NY), respectively. The physicochemical and biological characteristics of CuO and ZnO have been described by Eweje and colleagues,[28] while the 25 nm and 100 nm of TiO_2 have been characterized by Ahn et al.[29] and Lee et al.,[30] respectively. The Al_2O_3, Fe_2O_3, CeO_2, and WO_3 nanoparticles were synthesized via flame spray pyrolysis using the Harvard Versatile Engineered Nanomaterials Generation System (VENGES).[31] The synthesis and characterization of Al_2O_3, Fe_2O_3, and CeO_2 were detailed by Beltran-Huarac and colleagues.[32] The physicochemical and biological properties of MgO, V_2O_5, and WO_3 have been presented by our group previously.[13] All the nanomaterials used in this study had a near-spherical shape except V_2O_5, which was in the form of a nanoflake. Primary particle diameters as measured by transmission electron microscopy and specific surface area as measured by Brunauer-Emmett-Teller (BET) method are summarized in Supplement A.

Before use, resuspended ENMs were sonicated using a calibrated sonication system (2510R-MT; Branson Ultrasonics, Danbury, CT) following the protocol described by DeLoid and colleagues.[33] In brief, each ENM was placed into a 15 ml conical tube and deionized water (DW) was added to achieve a final concentration of 2.5 mg/ml. Next, the nanosuspensions were vortexed at high speed for 30 seconds and sonicated for ~3 to 6 minutes as detailed for each material (Supplement B). Following sonication, the stock suspensions were vortexed again for at least 30 seconds at high speed and diluted with culture media or balanced salt solution (BSS; Alcon, Geneva, Switzerland) to the final concentration. All diluted suspensions were used immediately after preparation and all preparation procedures were repeated every 24 hours. The stability of metal oxide nanomaterials in suspension was

tested with dynamic light scattering (DLS). The hydrodynamic diameter and polydispersity index were measured using a DLS instrument (Zetasizer Nano S90, Malvern Instruments Ltd., Malvern, UK) at 1 and 24 hours after preparation. (Supplement B).

Cell Culture

Primary rabbit corneal fibroblasts (RCFs) were isolated as previously described[34,35] and used between passages 3 and 7. The cells were cultured in Dulbecco's modified Eagle's medium (DMEM) low glucose (HyClone; GE Healthcare Life Sciences, Logan, UT) supplemented with 10% fetal bovine serum (FBS; Atlanta Biologicals, Lawrence, GA) and 1% penicillin-streptomycin-amphotericin B (PSF; Lonza, Walkersville, MD). RCFs were plated on a 6-well plate at a density of 1.5×10^5 per 2 ml of culture medium for PCR and western blot and left to adhere for 24 hours. The following day, the media was changed to growth media containing 0 or 10 ng/ml TGF-β1 with ENM or distilled water (vehicle control); 10 ng/ml of TGF-β1 has been previously shown to induce myofibroblast transformation in rabbit and human fibroblasts.[34,35] For PCR analysis, cells were harvested after the 24-hour incubation. For western blot analysis, after 24-hour incubation, cells were cultured in fresh media containing TGF-β1 (0 or 10 ng/ml) without ENMs for another 48 hours.

Cell Viability Assays

The impact of the 11 metal oxide ENMs on the viability of RCFs was determined using MTT [3-(4,5-dimethylthiazol-2-yl)-2,5-diphenyltetrazolium bromide] and Calcein AM (acetoxymethyl) assays. For the MTT assay, RCFs were seeded into a 96-well plate at a concentration of 2000 cells per 100 µl of culture medium and allowed to attach overnight. The cells were then treated for 24 hours with different concentrations of NPs ranging from 0.05 to 250 µg/ml in six replicates in the absence of TGFβ-1. Citrate-stabilized Au NPs (14 nm) show low or no toxicity in vitro,[36] so we used citrate-capped Au NPs (15 nm; 5 µg/ml) as a negative control. Saponin (1 mg/ml) and distilled water were used as positive and vehicle controls, respectively. Then, 10 µl MTT solution (5 mg/ml in PBS) was added to each well and the cells were incubated at 37°C for 3 hours. The media containing MTT solution was replaced with 125 µl dimethyl sulfoxide (DMSO) to dissolve the insoluble formazan crystals and absorbances were measured at 570 nm using a microplate reader (Synergy 4; BioTek Instruments, Inc., Winooski, VT). For the Calcein AM assay, RCFs were seeded at a density of 2000 cells per well and were incubated overnight in black-walled 96-well plates in 100 µl of culture medium. The media was removed and replaced with a 1 mM solution of Calcein AM in PBS the following day. The cells were incubated for 30 minutes at 37°C, and the fluorescence was measured with a 490 nm excitation filter and a 520 nm barrier filter using the microplate reader. All viability tests were performed in triplicate. Wells without cells were used as blank controls. The relative cell viability (%), relative to vehicle control wells, was calculated by (absorbance of treated cells − absorbance of blank)/(absorbance of vehicle control − absorbance of blank) × 100.

RNA Extraction and Quantitative Real-Time PCR

RCFs were plated on a 6-well plate at a density of 1.5×10^5 per 2 ml of culture medium and left to adhere for 24 hours. The following day, the media was changed to growth media containing 0 or 10 ng/ml TGF-β1 with ENM or distilled water (vehicle control); 10 ng/ml of TGF-β1 has been previously shown to induce myofibroblast transformation in rabbit and human fibroblasts.[34,35] Total RNA was extracted from RCFs at 24 hours after treatment with TGF-β1 (0 or 10 ng/ml) and ENMs or vehicle control using the GeneJET RNA Purification Kit (Thermo Fisher Scientific, Waltham, MA) following the manufacturer's specifications. The RNA was quantified by measuring its absorbance at 260 nm using a NanoDrop ND-1000 spectrophotometer (Thermo Fisher Scientific). Quantitative real-time PCR was performed using the SensiFAST Probe Hi-ROX One-Step kit (Bioline, Taunton, MA) and TaqMan aptamers specific to human glyceraldehyde 3-phosphate dehydrogenase (GAPDH, Oc03823402_g1; Thermo Fisher Scientific) or αSMA (ACTA2, Oc03399251_m1; Thermo Fisher Scientific) in total volume 10 µl per reaction as previously described[34]; GAPDH expression (a housekeeping gene) served as a control. Experiments were repeated at least three times. Gene expression data were calculated as previously reported[37] and normalized relative to the expression of mRNA from cells in the absence of both TGF-β1 and ENMs.

Protein Extraction and Western Blot

RCFs were plated on a 6-well plate at a density of 1.5×10^5 in culture medium and left to adhere overnight. The following day, the media was changed

to growth media containing 0 or 10 ng/ml TGF-β1 with ENM or distilled water. After 24 hours, cells were cultured in fresh media containing 0 or 10 ng/ml TGF-β1 without ENMs for another 48 hours. Protein was extracted using a radioimmunoprecipitation assay (RIPA) buffer and Protease/Phosphatase Inhibitor Cocktail (Thermo Fisher Scientific). Equivalent amounts of protein (10 µg) were loaded onto a 10% NuPAGE Bis-Tris gel (Life Technologies, Carlsbad, CA). Gel electrophoresis was performed at 100 mA for 35 minutes per gel, followed by transfer to a nitrocellulose membrane (Life Technologies) at 1.3 A for 10 minutes. The membrane was blocked at 37°C for 1 hour with a blocking buffer containing 80% PBS, 10% FBS, and 10% Superblock (Thermo Fisher Scientific). The membrane was incubated with a primary antibody specific to anti-αSMA (A5228; Sigma-Aldrich) diluted 1:5000 in a blocking buffer at 37°C for 1 hour. The blot was washed three times in TBS with 0.1% Tween-20 (TBS-T) before incubating with peroxidase-conjugated goat anti-mouse antibody (KPL, Gaithersburg, MD) diluted 1:20,000 in a blocking buffer at 37°C for 1 hour. After washing twice with TBS-T and once with TBS, protein bands of interest were detected using a western blotting detection kit (WesternBright Quantum, Advansta, Menlo Park, CA) and Sapphire Biomolecular Imager (Azure Biosystems, Dublin, CA). The same blot was stripped with Restore™ Western Blot Stripping Buffer (Thermo Fisher Scientific) for 20 minutes at room temperature and reproved with anti-GAPDH (G8795; Sigma-Aldrich) diluted 1:2000 in blocking buffer at 37°C for 1 hour as a reference protein. Densitometry analyses were done with ImageJ software (National Institutes of Health, Bethesda, MD). The band densities of αSMA were normalized to the values of GAPDH. Western blot analyses were performed on samples from at least three independent experiments.

Animals

Twelve New Zealand White female rabbits (Charles River Laboratories, Wilmington, MA) were used in this study with a mean ± SD bodyweight of 3.7 ± 0.1 kg. The study was approved by the Institutional Animal Care and Use Committee of the University of California, Davis (IACUC #19691) and performed in compliance with the Association of Research in Vision and Ophthalmology statement for the use of animals in vision research. A detailed ophthalmic examination was performed before inclusion in the study. Only animals without ocular disease were included in the study.

Phototherapeutic Keratectomy and Postoperative Treatment

Rabbits premedicated with intramuscular (IM) injection of midazolam (0.7 mg/kg) and hydromorphone (0.1 mg/kg) were anesthetized using an IM injection of ketamine (15–30 mg/kg) followed by isoflurane (1%–4%) inhalation. The surgical area was disinfected with 0.2% povidone-iodine solution. The cornea of the right eye (OD) was treated with 0.5% proparacaine hydrochloride ophthalmic solution (Alcon) and a central zone marked with an 8 mm trephine (MSI Instruments, Phoenixville, PA). The epithelium within the marked area was then debrided using an excimer spatula (Beaver-Visitec International, Inc, Waltham, MA) followed by a PTK (6 mm diameter, 40 Hz, 250 pulses, 100 µm depth) using a NIDEK EC-5000 excimer laser (Nidek Co. Ltd, Gamagori, Japan) as described previously.[38] The left eye remained unwounded and served as a control. Atropine sulfate ophthalmic solution 1% (Akorn, Inc., Lake Forest, IL) and ofloxacin 0.3% ophthalmic solution (Alcon) were administrated OD following the PTK treatment. Buprenorphine (0.04 mg/kg) was administered subcutaneously for postoperative analgesia. Rabbits were randomly assigned to receive 40 µl of BSS ($n = 6$, vehicle control) or Fe_2O_3 NP (250 µg/ml) in BSS ($n = 6$) in both eyes six times a day.

Ophthalmic Examination Scoring and Imaging

The semiquantitative preclinical ocular toxicology scoring (SPOTS) system[39] was employed to evaluate the anterior segment using a portable slit lamp (SL-15; Kowa Co. Ltd., Nagoya, Japan). Rebound tonometry (TonoVet; Icare, Helsinki, Finland) and Fourier-domain optical coherence tomography (FD-OCT; RTVue 100, software version 6.1; Optovue Inc, Fremont, CA) were also performed on days 1, 3, 7, 14, 21, and 28 following PTK treatment. Stromal haze thickness as reflected by a hyperreflective zone in the OCT image was measured manually using the caliper function integrated into the OCT software as described previously.[40] Fluorescein stain (HUB Pharmaceuticals, LLC, Rancho Cucamonga, CA) was performed to assess epithelial wound area twice daily with digital photography (Nikon D300). The remaining wound area at each time point was measured using ImageJ software (version 1.52k) and compared with the baseline wound area for each rabbit, and the percentage of the remaining wound area was calculated for each time point.

Tissue Harvest, Processing, and Immunohistochemistry

Rabbits were euthanized by intravenous injection of pentobarbital (100 mg/kg) and both eyes were removed for immunohistochemical examination. Enucleated eyes were fixed in 10% neutral buffered formalin, paraffin-embedded and sectioned at 5 µm. Sections were deparaffinized in xylene, subjected to citrate buffer (pH 6.0) for heat-induced epitope retrieval, peroxidase-blocked, and incubated with mouse anti-αSMA (A5228; 1:100 dilution, Sigma-Aldrich) antibody overnight at 4°C. Sections were then stained with goat anti-mouse secondary antibody conjugated to Alexa Fluor 488 (1:250 dilution, Thermo Fisher Scientific), followed by nuclear counterstaining with DAPI, and coverslipped. There was no staining when the secondary antibody was used alone as a negative control. Slides containing a globe section from each rabbit were imaged along the whole length of the cornea using a Leica DMi8 fluorescence microscope (Leica Microsystems, Buffalo Grove, IL). Corrected total cell fluorescence (CTCF) was calculated using the following formula, with the data from fluorescence microscopy images, using ImageJ software: CTCF = integrated density – (area of selected cell × mean fluorescence of background readings).

Statistical Analysis

Data were presented as mean ± standard deviation (SD) and statistical analyses were performed with GraphPad Prism 8 (GraphPad Software, San Diego, CA). All data sets were compared with Student's *t*-test using Welch's correction, or one-way analysis of variance (ANOVA), followed by a Dunnett's multiple comparisons test as indicated. Significance was defined as $P < 0.05$ for all analyses. Statistically significant differences are indicated in figures as $*P < 0.05$, $**P < 0.01$ or $***P < 0.001$, unless stated otherwise.

Results

ENMs Differentially Decreased Cell Viability

For the 11 metal oxide ENMs tested, the results from MTT and Calcein AM assays were remarkably consistent except TiO_2 (Fig. 1). The CeO_2 (10 nm) and WO_3 NPs showed mild toxicity at the highest concentration tested (250 µg/ml) in one or both assays. By contrast, V_2O_5, Fe_2O_3, CuO, and ZnO ENMs showed greater toxicity with cell viabilities less than 80% at the highest concentration (250 µg/ml). Interestingly, TiO_2 (100 nm) NPs at concentrations (≥25 µg/ml) showed significantly greater cell viability compared to vehicle control with Calcein AM but not MTT assays. Automated cell counting was performed using cells treated with vehicle or TiO_2 (100 nm) NPs (250 µg/ml) for 24 hours and demonstrated that cell viability was decreased by 51% in comparison to vehicle control consistent with the MTT assay (Supplement C).

TGF-β1-Induced αSMA mRNA Expression Was Decreased by V_2O_5 Nanoflakes and Increased by Fe_2O_3 NPs, but Only V_2O_5 Nanoflakes Altered αSMA Protein expression in the Presence of TGF-β1

We studied the effects of the 11 metal oxide ENMs on αSMA mRNA expression using quantitative real-time PCR (Fig. 2A). While most ENMs showed no significant change ($P > 0.05$) in αSMA mRNA expression in the absence or presence of TGF-β1, αSMA mRNA was significantly decreased ($P < 0.01$) in V_2O_5 nanoflake treated cells and significantly increased ($P < 0.001$) in Fe_2O_3 NP treated cells in the presence of TGF-β1. Western blot analyses were also performed on RCF lysates to measure the expression of αSMA, which was significantly decreased ($P < 0.01$) by V_2O_5 nanoflake but not altered ($P > 0.05$) by Fe_2O_3 NP in the presence of TGF-β1 (Figs. 2B and 2C).

Fe_2O_3 NP Showed No Effects on Stromal Haze Formation Following PTK Treatment

Epithelial wound closure did not differ between the Fe_2O_3 NP- and BSS-treated groups at all time points. (Figs. 3A and 3B). Stromal haze thickness as measured by FD-OCT (Fig. 3C) was significantly altered over time ($P < 0.001$) but did not differ between groups at any time point ($P > 0.05$; Fig. 3D). Using immunohistochemistry, αSMA protein expression in the stroma (Fig. 3E) did not markedly differ between groups at 28 days following PTK treatment ($P = 0.686$; Fig. 3F). Conjunctival hyperemia, swelling, and discharge, corneal opacity, and uveitis were assessed in all PTK-treated eyes until re-epithelialization using the SPOTS system, with no significant differences being found between groups ($P > 0.05$; data not shown).

Discussion

This study investigated in vitro effects of 11 metal oxide ENMs on cytotoxicity and KFM transformation of corneal stromal cells. Both CuO and ZnO NPs

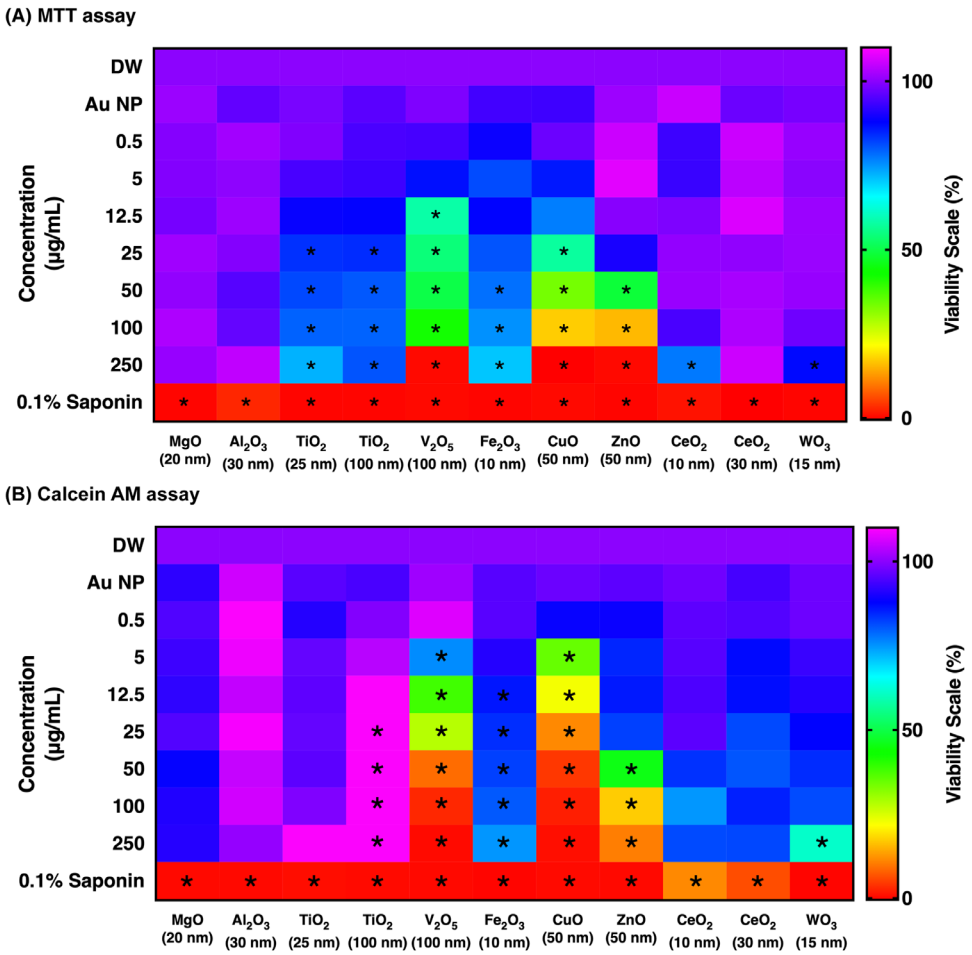

Figure 1. Rabbit corneal fibroblast cell viability was markedly reduced following treatment with some metal oxide ENMs. The MTT (**A**) and calcein AM (**B**) assays exhibited similar cell viability results for 11 metal oxide ENMs except for TiO_2. The V_2O_5, Fe_2O_3, CuO, and ZnO ENMs exerted more potent cytotoxic effects than the other metal oxide ENMs. The heatmaps represent corneal fibroblast cell viability percentage relative to vehicle control. In the heatmaps, *purple* and *red* indicate a high and low percentage of cell viability. $^*P < 0.05$, one-way ANOVA followed by Dunnett's multiple comparisons test was performed to compare with the vehicle (DW) controls. DW, deionized water; Au NP, gold nanoparticle; MgO, magnesium oxide; Al_2O_3, aluminum oxide; TiO_2, titanium dioxide; Fe_2O_3, iron(III) oxide; CuO, copper(II) oxide; ZnO, zinc oxide; CeO_2, cerium(IV) oxide; WO_3, tungsten trioxide.

release abundant metal ions and their cytotoxic effects are primarily due to this phenomenon.[5,21] Thus, it was unsurprising that CuO and ZnO NPs exhibited marked cytotoxicity to corneal fibroblasts consistent with previous studies in other ocular cells types including human corneal limbal epithelial cells and fibroblasts,[14] lens epithelial cells,[41] retinal ganglion cells,[42] and retinal photoreceptors.[43] Although CuO and ZnO NPs decreased cell viability and delayed epithelial and fibroblast migration in the present as well as previous studies,[13,14] they did not appear to alter KFM transformation in vitro at the concentrations tested. However, ZnO NPs delayed corneal epithelial migration in vivo and prior studies reported that they induced pulmonary fibrosis and increased myofibroblast expression in vivo,[13,44–50] suggesting that further in vitro and in vivo studies are warranted.

We determined that V_2O_5 nanoflakes were moderately toxic to RCFs, consistent with our previous study of corneal epithelial cells in vitro[13] as well as other studies on mammalian cells with V_2O_3 nanotubes, V_2O_5 NPs, and V_2O_5 nanotubes.[51–53] In aggregate, these data suggest that nanosized vanadium oxide materials are noxious to cells regardless of their shape or oxidation state. Occupational inhalation exposure to V_2O_5 increases the risk of obstructive lung disease[54] as these ENMs induce pulmonary inflammation and fibrosis in mice and rats.[55,56] Unexpectedly, a low concentration of V_2O_5 nanoflakes reduced mRNA and protein expression of αSMA in vitro consistent

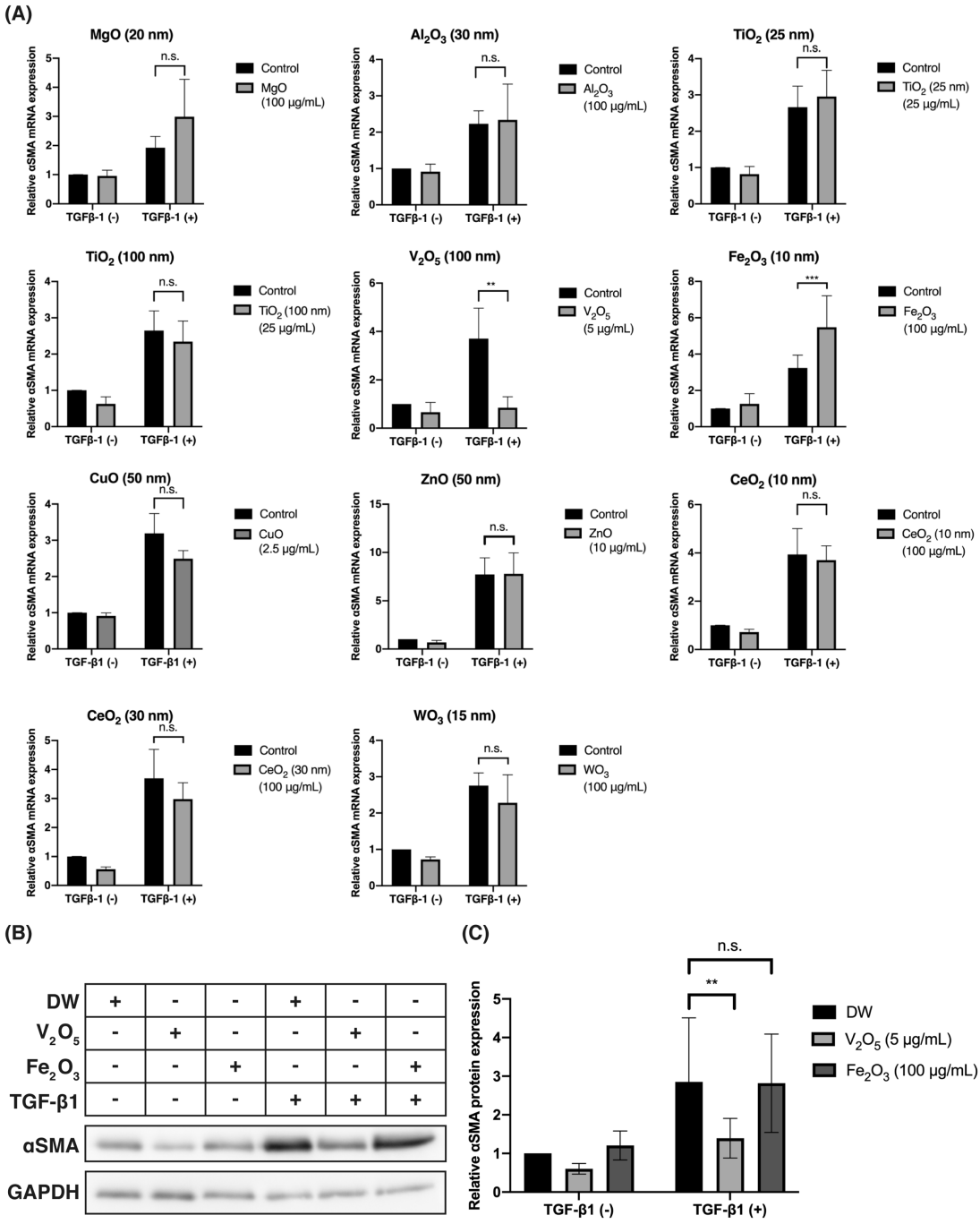

Figure 2. The V_2O_5 nanoflake decreased and Fe_2O_3 NP increased TGF-β1-induced mRNA expression of αSMA, but only V_2O_5 nanoflake significantly altered αSMA protein expression. (**A**) Gene expression of αSMA was analyzed by quantitative real-time PCR with normalization against GAPDH. (**B**) Representative western blot images showing the expression of αSMA and GAPDH. (**C**) Protein expression of αSMA was analyzed by western blotting with normalization against GAPDH. The data represent mean $\pm$ SD. $n \geq 3$. $^{**}P < 0.01$, $^{***}P < 0.001$, one-way ANOVA followed by Dunnett's multiple comparisons test was performed to compare with TGF-β1 treatment only.

with other studies of metal oxide ENMs that reduce fibrosis.[57,58] V_2O_5 nanoflakes delayed corneal epithelial migration in vitro but did not impact corneal epithelial wound healing in vivo in a rabbit model.[13] Therefore, V_2O_5 nanoflakes warrant further investigation to explore their potential as a therapeutic agent for preventing stromal haze formation following injury or surgery.

We identified mildly reduced corneal fibroblast cell viability following exposure to Fe_2O_3 NPs. Consistent with these findings, previous studies have shown that Fe_2O_3 NPs exhibit mild toxicity on human

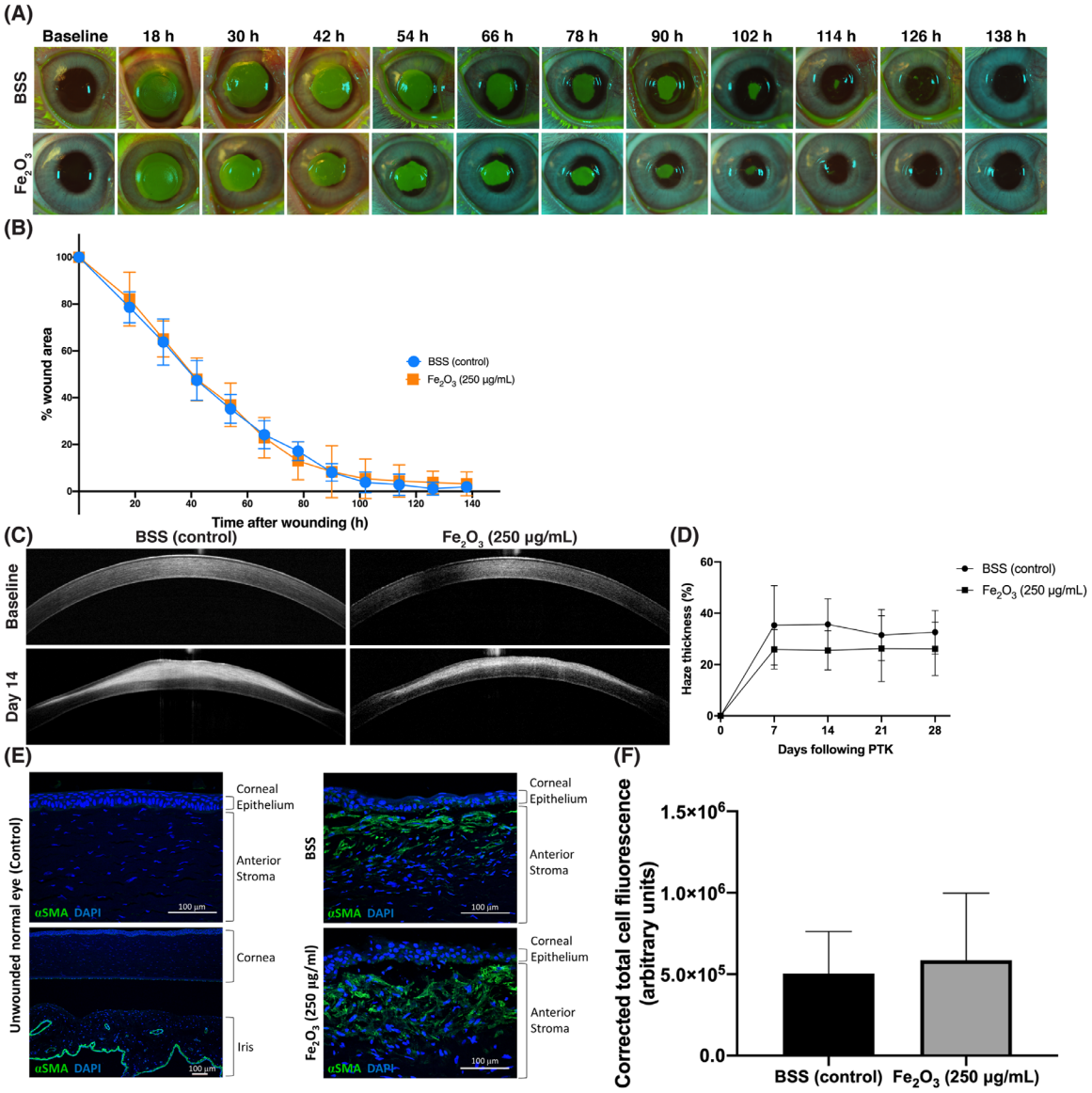

Figure 3. Stromal haze formation and αSMA expression did not significantly differ between rabbits treated with topical Fe_2O_3 NP or vehicle control (BSS). (**A**) Representative images of corneal epithelial wound healing in rabbits treated with topical Fe_2O_3 NP or BSS six times daily following a PTK. (**B**) No significant differences are identified between Fe_2O_3 and BSS treated groups at all time points. (**C**) Representative anterior segment SD-OCT images of the normal cornea (C, *top row*) and stromal haze (C, *bottom row*). At 14 days after PTK treatment, the hyperreflective stromal haze was observed in the central anterior stroma and was similar between groups. (**D**) Stromal haze thickness showed no significant differences between Fe_2O_3 NP- and BSS-treated groups at all time points. (**E**) Representative image of immunohistochemical staining for αSMA (*green*) in the central anterior stroma. Nuclei were stained with DAPI (*blue*). (**F**) Bar graph showing the averages of corrected total cell fluorescence (CTCF) for αSMA. No significant differences in the CTCF were observed between Fe_2O_3 NP- and BSS-treated groups. Data are represented as mean $\pm$ SD.

lung and bronchial cells by inducing oxidative stress, especially mitochondrial oxidative damage.[59–61] In TGF-β1-induced myofibroblasts, Fe_2O_3 NPs markedly increased in vitro mRNA expression of αSMA, but not protein. The cause of this incongruency is unknown, but it may be related to posttranslational modifications and/or protein degradation.[62,63] We also determined that topical Fe_2O_3 NPs did not affect corneal re-epithelialization or stromal haze formation in an in vivo study using a rabbit PTK model. This contrasts with a previous study of long-term inhalation exposure to Fe_2O_3 NPs which induced pulmonary fibrosis through a macrophage inflammatory response.[64] In aggregate, these data suggest that ocular exposure to Fe_2O_3 NPs should not impact corneal epithelial or stromal wound healing.

In conclusion, four ENMs (V_2O_5, Fe_2O_3, CuO, and ZnO) demonstrated greater toxicity to cultured RCFs in comparison to seven other metal oxide ENMs. The V_2O_5 nanoflakes attenuated KFM transformation in vitro, but further investigations are required to determine their impact on stromal wound healing. While Fe_2O_3 NPs induced KFM transformation in vitro, it did not impact stromal wound healing in vivo.

Acknowledgments

Funded by grants from NIEHS U01 ES027288, NEI R01 EY019970, and P30 EY012576. The engineered nanomaterials used in the research presented in this publication have been procured/developed, characterized, and provided by the Engineered Nanomaterials Resource and Coordination Core established at Harvard T. H. Chan School of Public Health (NIEHS U24ES026946) as part of the Nanotechnology Health Implications Research (NHIR) Consortium.

Disclosure: **A. Fukuto,** None; **S. Kim,** None; **J. Kang,** None; **B.L. Gates,** None; **M.W. Chang,** None; **K.E. Pinkerton,** None; **L.S. Van Winkle,** None; **Y. Kiuchi,** None; **C.J. Murphy,** None; **B.C. Leonard,** None; **S.M. Thomasy**, None

* AF and SK contributed equally to this article; authors listed in alphabetical order.

References

1. Kühnel D, Marquardt C, Nau K, Krug HF, Mathes B, Steinbach C. Environmental impacts of nanomaterials: providing comprehensive information on exposure, transport and ecotoxicity – the project DaNa2.0. *Environ Sci Eur*. 2014;26:21.
2. Bahrami B, Hojjat-Farsangi M, Mohammadi H, et al. Nanoparticles and targeted drug delivery in cancer therapy. *Immunol Lett*. 2017;190:64–83.
3. Solanki PR, Kaushik A, Agrawal VV, Malhotra BD. Nanostructured metal oxide-based biosensors. *NPG Asia Mater*. 2011;3:17–24.
4. Mehra NK, Cai D, Kuo L, Hein T, Palakurthi S. Safety and toxicity of nanomaterials for ocular drug delivery applications. *Nanotoxicology*. 2016;10:836–860.
5. Ivask A, Titma T, Visnapuu M, et al. Toxicity of 11 metal oxide nanoparticles to three mammalian cell types in vitro. *Curr Top Med Chem*. 2015;15:1914–1929.
6. Chusuei CC, Wu CH, Mallavarapu S, et al. Cytotoxicity in the age of nano: the role of fourth period transition metal oxide nanoparticle physicochemical properties. *Chem Biol Interact*. 2013;206:319–326.
7. Zhang H, Ji Z, Xia T, et al. Use of metal oxide nanoparticle band gap to develop a predictive paradigm for oxidative stress and acute pulmonary inflammation. *ACS Nano*. 2012;6:4349–4368.
8. Wang Y, Aker WG, Hwang HM, Yedjou CG, Yu H, Tchounwou PB. A study of the mechanism of in vitro cytotoxicity of metal oxide nanoparticles using catfish primary hepatocytes and human HepG2 cells. *Sci Total Environ*. 2011;409:4753–4762.
9. Jeng HA, Swanson J. Toxicity of metal oxide nanoparticles in mammalian cells. *J Environ Sci Health A Tox Hazard Subst Environ Eng*. 2006;41:2699–2711.
10. Chen J, Zhu J, Cho H-H, et al. Differential cytotoxicity of metal oxide nanoparticles. *J Exp Nanosci*. 2009;3:321–328, https://doi.org/10.1080/17458080802235765.
11. Eom Y, Song JS, Lee DY, et al. Effect of titanium dioxide nanoparticle exposure on the ocular surface: an animal study. *Ocul Surf*. 2016;14:224–232.
12. Lee H, Park K. In vitro cytotoxicity of zinc oxide nanoparticles in cultured statens seruminstitut rabbit cornea cells. *Toxicol Res*. 2019;35:287–294.
13. Kim S, Gates BL, Leonard BC, et al. Engineered metal oxide nanomaterials inhibit corneal epithelial wound healing in vitro and in vivo. *NanoImpact*. 2020;17:100198.
14. Zhou EH, Watson C, Pizzo R, et al. Assessing the impact of engineered nanoparticles on wound healing using a novel in vitro bioassay. *Nanomedicine (Lond)*. 2014;9:2803–2815.
15. Fini ME, Stramer BM. How the cornea heals: cornea-specific repair mechanisms affecting surgical outcomes. *Cornea*. 2005;24:S2–S11.
16. Jester JV, Petroll WM, Barry PA, Cavanagh HD. Expression of alpha-smooth muscle (alpha-SM) actin during corneal stromal wound healing. *Invest Ophthalmol Vis Sci*. 1995;36:809–819.
17. Jester JV, Huang J, Barry-Lane PA, Kao WW, Petroll WM, Cavanagh HD. Transforming growth factor(beta)-mediated corneal myofibroblast differentiation requires actin and fibronectin assembly. *Invest Ophthalmol Vis Sci*. 1999;40:1959–1967.
18. Jester JV, Petroll WM, Cavanagh HD. Corneal stromal wound healing in refractive surgery: the role of myofibroblasts. *Prog Retin Eye Res*. 1999;18:311–356.

19. Wilson SE, Mohan RR, Ambrosio R, Jr., Hong J, Lee J. The corneal wound healing response: cytokine-mediated interaction of the epithelium, stroma, and inflammatory cells. *Prog Retin Eye Res*. 2001;20:625–637.
20. Wehmas LC, Anders C, Chess J, et al. Comparative metal oxide nanoparticle toxicity using embryonic zebrafish. *Toxicol Rep*. 2015;2:702–715.
21. Wang D, Lin Z, Wang T, et al. Where does the toxicity of metal oxide nanoparticles come from: the nanoparticles, the ions, or a combination of both? *J Hazard Mater*. 2016;308:328–334.
22. Yang Y, Wang Z, Yang H, et al. TRPV1 potentiates TGFβ-induction of corneal myofibroblast development through an oxidative stress-mediated p38-SMAD2 signaling loop. *PLoS One*. 2013;8:e77300.
23. Koli K, Myllarniemi M, Keski-Oja J, Kinnula VL. Transforming growth factor-beta activation in the lung: focus on fibrosis and reactive oxygen species. *Antioxid Redox Signal*. 2008;10:333–342.
24. Samarakoon R, Overstreet JM, Higgins PJ. TGF-β signaling in tissue fibrosis: redox controls, target genes and therapeutic opportunities. *Cell Signal*. 2013;25:264–268.
25. Chavali MS, Nikolova MP. Metal oxide nanoparticles and their applications in nanotechnology. *SN Appl Sci*. 2019;1:607.
26. Turkevich J, Stevenson PC, Hillier J. A study of the nucleation and growth processes in the synthesis of colloidal gold. *Discuss. Faraday Soc*. 1951;11:55–75.
27. Dong J, Carpinone P, Pyrgiotakis G, Demokritou P, Moudgil B. Synthesis of precision gold nanoparticles using Turkevich method. *Kona*. 2020;37:224–232.
28. Eweje F, Ardona HAM, Zimmerman JF, et al. Quantifying the effects of engineered nanomaterials on endothelial cell architecture and vascular barrier integrity using a cell pair model. *Nanoscale*. 2019;11:17878–17893.
29. Ahn S, Ardona HAM, Lind JU, et al. Mussel-inspired 3D fiber scaffolds for heart-on-a-chip toxicity studies of engineered nanomaterials. *Anal Bioanal Chem*. 2018;410:6141–6154.
30. Lee JY, Wang H, Pyrgiotakis G, et al. Analysis of lipid adsorption on nanoparticles by nanoflow liquid chromatography-tandem mass spectrometry. *Anal Bioanal Chem*. 2018;410:6155–6164.
31. Demokritou P, Buchel R, Molina RM, Deloid GM, Brain JD, Pratsinis SE. Development and characterization of a versatile engineered nanomaterial generation system (VENGES) suitable for toxicological studies. *Inhal Toxicol*. 2010;22(Suppl 2):107–116.
32. Beltran-Huarac J, Zhang Z, Pyrgiotakis G, et al. Development of reference metal and metal oxide engineered nanomaterials for nanotoxicology research using high throughput and precision flame spray synthesis approaches. *NanoImpact*. 2018;10:26–37.
33. DeLoid GM, Cohen JM, Pyrgiotakis G, Demokritou P. Preparation, characterization, and in vitro dosimetry of dispersed, engineered nanomaterials. *Nat Protoc*. 2017;12:355–371.
34. Dreier B, Thomasy SM, Mendonsa R, Raghunathan VK, Russell P, Murphy CJ. Substratum compliance modulates corneal fibroblast to myofibroblast transformation. *Invest Ophthalmol Vis Sci*. 2013;54:5901–5907.
35. Myrna KE, Mendonsa R, Russell P, et al. Substratum topography modulates corneal fibroblast to myofibroblast transformation. *Invest Ophthalmol Vis Sci*. 2012;53:811–816.
36. Vetten MA, Tlotleng N, Tanner Rascher D, et al. Label-free in vitro toxicity and uptake assessment of citrate stabilised gold nanoparticles in three cell lines. *Part Fibre Toxicol*. 2013;10:50.
37. Thomasy SM, Raghunathan VK, Miyagi H, et al. Latrunculin B and substratum stiffness regulate corneal fibroblast to myofibroblast transformation. *Exp Eye Res*. 2018;170:101–107.
38. Raghunathan VK, Thomasy SM, Strom P, et al. Tissue and cellular biomechanics during corneal wound injury and repair. *Acta Biomater*. 2017;58:291–301.
39. Eaton JS, Miller PE, Bentley E, Thomasy SM, Murphy CJ. The SPOTS system: an ocular scoring system optimized for use in modern preclinical drug development and toxicology. *J Ocul Pharmacol Ther*. 2017;33:718–734, https://doi.org/10.1089/jop.2017.0108.
40. Raghunathan V, Edwards SG, Leonard BC, et al. Differential effects of Hsp90 inhibition on corneal cells in vitro and in vivo. *Exp Eye Res*. 2021;202:108362.
41. Wang D, Guo D, Bi H, Wu Q, Tian Q, Du Y. Zinc oxide nanoparticles inhibit Ca2+-ATPase expression in human lens epithelial cells under UVB irradiation. *Toxicol In Vitro*. 2013;27:2117–2126.
42. Guo D, Bi H, Liu B, Wu Q, Wang D, Cui Y. Reactive oxygen species-induced cytotoxic effects of zinc oxide nanoparticles in rat retinal ganglion cells. *Toxicol In Vitro*. 2013;27:731–738.
43. Guo DD, Li QN, Li CM, Bi HS. Zinc oxide nanoparticles inhibit murine photoreceptor-derived cell proliferation and migration via reducing TGF-$\beta$and MMP-9 expression in vitro. *Cell Prolif*. 2015;48:198–208.

44. Ko JW, Shin NR, Park JW, et al. Copper oxide nanoparticles induce collagen deposition via TGF-β1/Smad3 signaling in human airway epithelial cells. *Nanotoxicology*. 2018;12:239–250.
45. Lai X, Zhao H, Zhang Y, et al. Intranasal delivery of copper oxide nanoparticles induces pulmonary toxicity and fibrosis in C57BL/6 mice. *Sci Rep* 2018;8:4499.
46. Wang D, Li H, Liu Z, Zhou J, Zhang T. Acute toxicological effects of zinc oxide nanoparticles in mice after intratracheal instillation. *Int J Occup Environ Health*. 2017;23:11–19.
47. Juang Y-M, Chien H-J, Yang C-Y, Yeh H-C, Cheng T-J, Lai C-C. Comparative proteomic analysis of rat bronchoalveolar lavage fluid after exposure to zinc oxide nanoparticles. *Mass Spectrom (Tokyo)*. 2017;6:S0066–S0066.
48. Jacobsen NR, Stoeger T, van den Brule S, et al. Acute and subacute pulmonary toxicity and mortality in mice after intratracheal instillation of ZnO nanoparticles in three laboratories. *Food Chem Toxicol*. 2015;85:84–95.
49. Cho WS, Duffin R, Howie SE, et al. Progressive severe lung injury by zinc oxide nanoparticles; the role of Zn2+ dissolution inside lysosomes. *Part Fibre Toxicol*. 2011;8:27.
50. Jain S, Rachamalla M, Kulkarni A, Kaur J, Tikoo K. Pulmonary fibrotic response to inhalation of ZnO nanoparticles and toluene co-exposure through directed flow nose only exposure chamber. *Inhal Toxicol*. 2013;25:703–713.
51. Ivankovic S, Music S, Gotic M, Ljubesic N. Cytotoxicity of nanosize V(2)O(5) particles to selected fibroblast and tumor cells. *Toxicol In Vitro*. 2006;20:286–294.
52. Wörle-Knirsch JM, Kern K, Schleh C, Adelhelm C, Feldmann C, Krug HF. Nanoparticulate vanadium oxide potentiated vanadium toxicity in human lung cells. *Environ Sci Technol.* 2007;41(1):331–336.
53. Rhoads LS, Silkworth WT, Roppolo ML, Whittingham MS. Cytotoxicity of nanostructured vanadium oxide on human cells in vitro. *Toxicol In Vitro*. 2010;24:292–296.
54. Irsigler GB, Visser PJ, Spangenberg PAL. Asthma and chemical bronchitis in vanadium plant workers. *Am J Ind Med*. 1999;35:366–374.
55. Walters DM, White KM, Patel U, et al. Genetic susceptibility to interstitial pulmonary fibrosis in mice induced by vanadium pentoxide (V_2O_5). *FASEB J*. 2014;28:1098–1112.
56. Bonner JC, Rice AB, Moomaw CR, Morgan DL. Airway fibrosis in rats induced by vanadium pentoxide. *Am J Physiol Lung Cell Mol Physiol*. 2000;278:L209–L216.
57. Oro D, Yudina T, Fernandez-Varo G, et al. Cerium oxide nanoparticles reduce steatosis, portal hypertension and display anti-inflammatory properties in rats with liver fibrosis. *J Hepatol*. 2016;64:691–698.
58. Bashandy SAE, Alaamer A, Moussa SAA, Omara EA. Role of zinc oxide nanoparticles in alleviating hepatic fibrosis and nephrotoxicity induced by thioacetamide in rats. *Can J Physiol Pharmacol*. 2018;96:337–344.
59. Bhattacharya K, Davoren M, Boertz J, Schins RP, Hoffmann E, Dopp E. Titanium dioxide nanoparticles induce oxidative stress and DNA-adduct formation but not DNA-breakage in human lung cells. *Part Fibre Toxicol*. 2009;6:17.
60. Karlsson HL, Gustafsson J, Cronholm P, Moller L. Size-dependent toxicity of metal oxide particles–a comparison between nano- and micrometer size. *Toxicol Lett*. 2009;188:112–118.
61. Freyria FS, Bonelli B, Tomatis M, et al. Hematite nanoparticles larger than 90 nm show no sign of toxicity in terms of lactate dehydrogenase release, nitric oxide generation, apoptosis, and comet assay in murine alveolar macrophages and human lung epithelial cells. *Chem Res Toxicol*. 2012;25:850–861.
62. Vogel C, Marcotte EM. Insights into the regulation of protein abundance from proteomic and transcriptomic analyses. *Nat Rev Genet*. 2012;13:227–232.
63. Mohamed BM, Verma NK, Davies AM, et al. Citrullination of proteins: a common post-translational modification pathway induced by different nanoparticles in vitro and in vivo. *Nanomedicine (Lond)*. 2012;7:1181–1195.
64. Andujar P, Simon-Deckers A, Galateau-Sallé F, et al. Role of metal oxide nanoparticles in histopathological changes observed in the lung of welders. *Part Fibre Toxicol*. 2014;11:23.